Applied Catalysis B: Environmental 178 (2015) 210–217

Contents lists available at ScienceDirect

Applied Catalysis B: Environmental

journal homepage: www.elsevier.com/locate/apcatb

Modelling of the operation of raceway pond reactors for micropollutant removal by solar photo-Fenton as a function of photon absorption

G. Rivas[a,b], I. Carra[a,b], J.L. García Sánchez[a,b], J.L. Casas López[a,b], S. Malato[b,c], J.A. Sánchez Pérez[a,b,*]

[a] Department of Chemical Engineering, University of Almería, 04120 Almería, Spain
[b] CIESOL, Joint Centre of the University of Almería-CIEMAT, 04120 Almería, Spain
[c] Plataforma Solar de Almería (CIEMAT), 042[1]00 Tabernas, Almería, Spain

ARTICLE INFO

Article history:
Received 11 July 2014
Received in revised form 4 September 2014
Accepted 7 September 2014
Available online 16 September 2014

Keywords:
Acetamiprid
Thiabendazole
Photon absorption
Kinetic model
Treatment capacity

ABSTRACT

Raceway ponds reactors (RPRs) are extensive non-concentrating photoreactors which allow large volumes of water to be treated. They consist of channels where water is set in motion by a paddlewheel system. In this work the effect of solar irradiance on RPR operation to remove micropollutants by solar photo-Fenton was studied. A RPR was used at pilot plant scale (up to 360 L) and the pesticides acetamiprid (ACTM) and thiabendazole (TBZ) were used as a model pollutant mixture (100 μg/L each) in simulated effluent. Averaged UV irradiances ranged from 10 to 30 W/m^2 and three values of iron concentration (1, 5.5 and 10 mg/L) were used. Different liquid depths were also used to evaluate the relationship between the rate of photon absorption and pollutant removal. A model was proposed to predict degradation rate and treatment capacity as a function of the volumetric rate of photon absorption (VRPA). Under low irradiance conditions (10 W/m^2) the treatment capacity was not sensitive above 10 cm liquid depth, so a low iron concentration should be used (5 mg Fe/L). For high irradiance values (30 W/m^2), greater liquid depth (20 cm) and iron concentration (10 mg Fe/L) should be used to take full advantage of photon availability. Treatment capacity values of 133 mg/h m^2 can be reached under these conditions.

1. Introduction

There is an increasing environmental concern about organic contaminants found in waters at concentrations in the ng/L–μg/L range, named micropollutant [1–4]. They cover a great variety of organic compounds such as pharmaceuticals, personal care products and pesticides. They are released to wastewater effluents by anthropogenic activities, reaching wastewater treatment plants (WWTPs). However, conventional methods such as biological treatments are not enough to remove these compounds [5]. As a result, micropollutants continuously escape into the environment [6–8]. They can pose potential environmental risks. For instance, phenomena such as bioaccumulation or hermaphroditism in fish have been reported in recent years due to DNA alterations by endocrine disruptors [9,10]. Consequently, research is being developed to remove them by including a tertiary stage in WWTPs. In this regard, advanced oxidation processes (AOPs) have been widely used due to their efficiency in recalcitrant pollutant mineralisation to CO_2 and H_2O [11]. They are based on the generation of oxidative radicals which oxidise organic compounds. Amongst them, the photo-Fenton process has proved to be effective in micropollutant removal [12]. Specifically, this process is based on the redox iron cycle to generate hydroxyl radicals ($HO^\bullet$) ($E_0 = -2.8$ V). In summary, iron acts as catalyst and is oxidised and reduced cyclically: ferrous iron (Fe^{2+}) reacts with hydrogen peroxide, yielding hydroxyl radicals and is oxidised to ferric iron. Subsequently, ferric iron can absorb light in the UV–vis range, also yielding hydroxyl radicals and reducing it to ferrous iron again. Consequently, this process is strongly dependent on iron concentration and irradiance and both are important factors in reactor design and process operation [13,14].

The absorption of irradiance by the catalyst is greatly affected by light distribution inside the photoreactor and therefore has a direct influence on the process kinetics [15,16]. As such, photoreactor configuration is critical. To remove pollutants in the

* Corresponding author at: Department of Chemical Engineering, University of Almería, 04120 Almería, Spain. Tel.: +34 950015314; fax: +34 950015484.
E-mail address: jsanchez@ual.es (J.A. Sánchez Pérez).

http://dx.doi.org/10.1016/j.apcatb.2014.09.015
0926-3373/

mg/L–g/L range (macropollutants), tubular compound parabolic collectors (CPCs) are the most optimised photoreactors for solar-driven photo-Fenton [17]. They make the most out of the beams reaching the reactor surface and allow generating high concentration of hydroxyl radicals working with solar irradiation. A drawback of this system though, is that they do not have a good efficiency when working with low concentration of contaminants needing low concentration of hydroxyl radicals as the ratio treated volume/surface is low. Photoreactor diameter (light path length) is in the range of a few cm for optimising costs of solar collector, glass tube and pressure drop and under these conditions optimal Fe concentration for maximising photons absorption is in the range of 0.2–0.3 mM [14]. Under these conditions, too high concentration of radicals would be produced for removing microcontaminants and therefore an important part of them would be wasted. Therefore, to remove pollutants in the μg/L–ng/L range (micropollutants) by solar-driven photo-Fenton, CPCs seems not to be the best choice.

Therefore, photoreactors with less efficient optics but a larger treated volume/surface ratio (i.e., longer light path length) could be used [18]. The light path length can be enlarged only by increasing the liquid depth in very simple photoreactors like solar ponds. In this way, raceway pond reactors (RPRs) could provide a good alternative for micropollutant degradation. They consist of open channels forming a raceway where the liquid is set in motion by a paddlewheel. They have been used for a long time for solar applications like microalgal mass culture [19] and are enough developed from an engineering point of view [20]. They allow wider optical paths (proportional to liquid depth in the photoreactor) than tubular photoreactors, so more volume can be treated per surface unit. Nevertheless, the appropriate optical path depends on liquid depth, iron concentration and irradiance distribution in the reactor. Indeed, liquid depth could be used as an operation variable and set as a function of solar irradiance.

This work was aimed at studying the effect of solar irradiance on RPR operation to remove micropollutants with solar photo-Fenton at pilot plant scale. For this purpose, a mixture of commercial pesticides, acetamiprid (ACTM) and thiabendazole (TBZ), 100 μg/L each, was used in simulated secondary effluent of municipal wastewater treatment plant (MWTP) as a model pollutant mixture, avoiding the disturbance of daily variations in real effluents. Both pesticides are commonly applied to citrus crops in the Mediterranean area. Outdoor experiments were carried out from February to May 2014, at two liquid depths, 5 cm and 15 cm, which corresponded to 120 L and 360 L water volume. Averaged UV irradiances ranged from 10 to 30 W/m^2. Three values of iron concentration (1, 5.5 and 10 mg/L) were used to study the relationship between the rate of photon absorption and pollutant removal.

2. Materials and methods

2.1. Chemicals

Sulphuric acid (95–97%) and hydrogen peroxide (35%) were obtained from J.T. Baker and ferrous sulphate (99%) from Fluka. $CaSO_4{\cdot}2H_2O$, $MgSO_4$, KCl, $(NH_4)_2SO_4$, $NaHCO_3$, beef extract, peptone, humic salts, sodium lignin sulfonate, sodium lauryle sulphate, acacia gum powder, formic acid and Arabic acid were acquired from Sigma–Aldrich. Commercial formulations of pesticides were used: EPIK® (20% (w/w) ACTM) and TEXTAR® (60% (w/v) TBZ). HPLC grade acetonitrile from Carlo Erba Reagents and Milli-Q grade water were used in the chromatographic analysis.

2.2. Experimental set-up

The experiments were carried out in a fibreglass-RPR pilot plant in the Centre for Solar Energy Research (CIESOL) in Almería, Spain. A

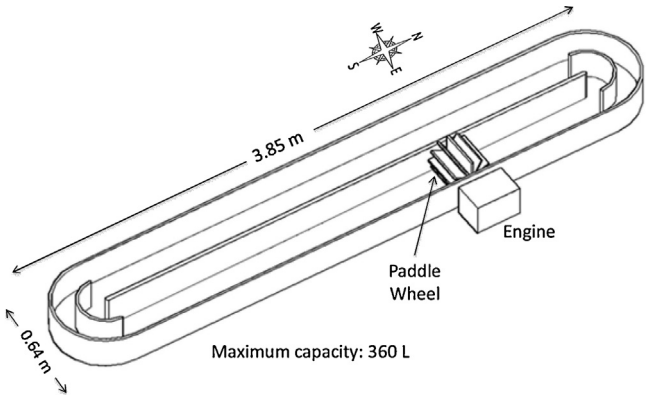

Fig. 1. RPR scheme.

pH value of 2.8 was chosen because it is the optimum for the photo-Fenton process [21] and allows a higher solubility of iron, allowing evaluating properly the efficiency of RPRs. Future work will be focused on working at circumneutral pH in RPRs, recommended to treat micropollutants [22]. The fibreglass-RPR has a maximum capacity of 360 L, a length of 3.85 m and width of 0.64 m. It is separated by a central wall, forming two channels. The RPR includes a paddlewheel connected to an engine to obtain a mixed and homogeneous flow during the process. The engine was linked to a variable frequency drive to control the paddles' speed. A scheme of the plant is presented in Fig. 1. The Reynolds number was estimated for each liquid height and a turbulent regime was used: 6×10^5 and 7×10^5 for 5 cm and 15 cm liquid depth, respectively.

Iron concentration and liquid depth (treated volume) were the process variables studied. Iron concentration was kept to low values, 1, 5.5 and 10 mg/L, typically used for micropollutant removal [12,23]. Low concentrations of iron contribute to prevent large generation of iron sludge when neutralising the effluent after the treatment. Initial hydrogen peroxide concentration was 50 mg/L to work in oxidant excess conditions. Liquid depth, which determines irradiance path length, was 5 cm and 15 cm. The first value was taken as the common diameter (light path length) used in tubular reactors of CPCs [16]. The last depth value is the maximum allowed by the configuration of the RPR reactor. As the liquid depth changes, so does the treated water volume in each case. To ensure similar mixing times the paddlewheel speed was changed according to the treated volume and mixing time was experimentally measured by means of a pulse test with a tracer. The result was a ~2.5 min mixing time for all cases.

UV radiation was measured using a global UV radiometer (Delta Ohm, LP UVA 02 AV) with a spectral response range from 327 to 384 nm, mounted on a horizontal platform, providing data in terms of incident UV radiation (W/m^2). The experiments were run in the central hours of the day to have the minimum variation in solar radiation under stable weather conditions.

The plant was equipped with pH and temperature probes. The variables were monitored on-line by means of a LabJack USB/Ethernet data acquisition device connected to a computer. Prior to the beginning of the experiments, the reactor was covered and pH was adjusted to 2.8 ± 0.05 with sulphuric acid. A recirculation time of 5 min was allowed for homogenisation after the addition of the pesticide mixture and iron salt, corresponding to twice the mixing time in the photoreactor.

Both ACTM and TBZ are commonly used in citrus crops which predominate in the Mediterranean agriculture (e.g. lemon, orange trees) [24,25]. ACTM is a neonicotinoid insecticide and it has been reported to be more resistant to oxidation than other pollutants typically found in WWTP effluents [18,26]. TBZ is a widely used

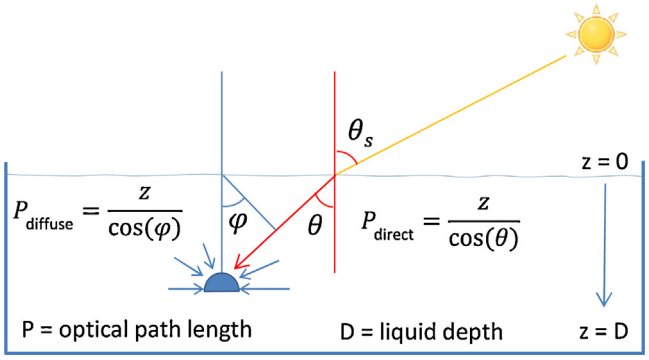

Fig. 2. Schematic view of raceway with direct and diffuse light paths.

benzimidazole fungicide. Thus, ACTM and TBZ at 100 μg/L each serve the purpose of model pollutants.

Experiments were carried out in simulated secondary effluent from an urban WWTP. The constituents of the simulated secondary effluent were: $CaSO_4{\cdot}2H_2O$ (60 mg/L), $MgSO_4$ (60 mg/L), KCl (4 mg/L), $(NH_4)_2SO_4$ (23.6 mg/L), K_2HPO_4 (7.0 mg/L), $NaHCO_3$ (96 mg/L), beef extract (1.8 mg/L), peptone (2.7 mg/L), humic salts (4.2 mg/L), sodium lignin sulfonate (2.4 mg/L), sodium lauryle sulphate (0.9 mg/L), acacia gum powder (4.7 mg/L), and Arabic acid (5.0 mg/L) [27]. The dissolved organic carbon concentration, DOC, was over 14 mg/L.

2.3. Solar radiation field and VRPA estimation

Global UV radiation in the 327–384 nm range (spectral response of the UV radiometer) was tracked and registered for each experimental run. This irradiance is composed of a fraction of direct irradiance and another fraction of diffuse irradiance. The former has an optical light path which depends on the incident angle on the reactor surface. The latter, comes from all directions from above the point considered, as depicted in Fig. 2.

The angle of incidence of a solar beam on water surface, θ_S, (Fig. 2) is a straightforward computation from Duffie–Beckman correlations [28], once the geographical location of the reactor, day of the year and time of the day are given. Due to refraction, the angle of incidence inside the reactor, θ, (Fig. 2) changes following the Snell law. In this case, 1.33 was assumed as refraction index for the used water matrix.

Regarding the absorption of the incident radiation, the ferric iron species in solution are dominant for UV-light absorption as hydrogen peroxide and ferrous iron do not absorb any radiation over 300 nm [29,30]. Absorption of acetamiprid, thiabendazole and generated intermediates was checked and found negligible over 300 nm at the concentration used in the experiments.

The UV absorption spectra of Fe (III) solutions in simulated secondary effluent were evaluated and the spectral-averaged specific absorption coefficient k_A ($mM^{-1}\,m^{-1}$) of solution species was determined, Eq. (1).

$$k_A = \frac{\int_{\lambda_{min}}^{\lambda_{max}} \varepsilon_\lambda I_\lambda d\lambda}{\int_{\lambda_{min}}^{\lambda_{max}} I_\lambda d\lambda} \quad (1)$$

where I_λ is the solar irradiance at the corresponding wavelength (W/m^2) and ε_λ is the specific absorption coefficient of the solution at the corresponding wavelength ($mM^{-1}\,m^{-1}$). The wavelength limits in Eq. (1) were those corresponding to radiometer spectral response (327–384 nm). The specific absorption coefficient for ferric iron species at pH 2.8 in simulated secondary effluent was 51 $mM^{-1}\,m^{-1}$.

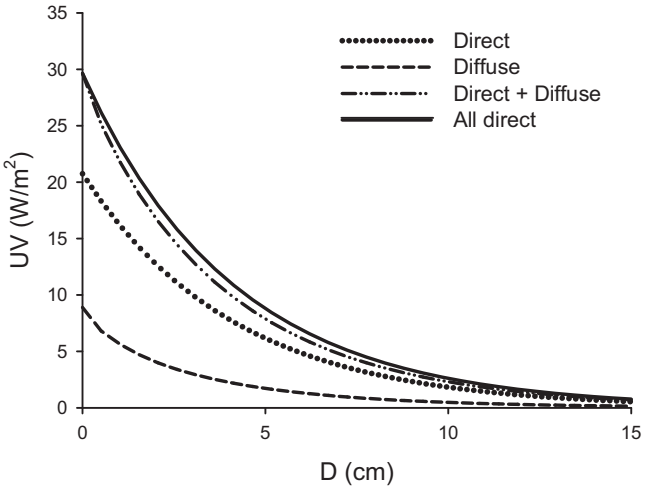

Fig. 3. Comparison of light profiles inside the reactor: $UV_o = 30\,W/m^2$. $UV_{direct} = 0.7\,UV_o$ and $UV_{diffuse} = 0.3\,UV_o$.

The attenuation of direct UV radiation is a function of the iron concentration and light path length as described in Fig. 2:

$$I_{direct}(z) = UV_{direct}\,10^{-(k_A \cdot C_{Fe} \cdot (z/\cos\theta))} \quad (2)$$

As for diffuse radiation, it was assumed that all directions have the same contribution (isotropic model) and symmetry with zenith. With these assumptions, the attenuation of this component as it penetrates the liquid bulk in the reactor is expressed as:

$$I_{diffuse}(z) = \int_{-\pi/2}^{\pi/2} UV_{diffuse}\,10^{-(k_A \cdot C_{Fe} \cdot (z/\cos\varphi))} d\varphi \quad (3)$$

To account for the solar UV fractions, direct and diffuse, a first approximation was made considering that all irradiance reaching the reactor surface was direct and it was then compared to the attenuation with the normal values of fractioned radiation, e.g. 70% direct and 30% diffuse, for a clear day. This calculation is shown in Fig. 3, where the sum of the two irradiance fractions calculated with the respective equations equals the suggested approximation.

Assuming clear day condition avoids the need of fraction estimation as UV is already available and only Eq. (2) would be used for light absorption inside the reactor with UV instead of UV_{direct}.

Based on the above discussion on light attenuation, the volumetric rate of photon absorption (VRPA) in the photochemical reactor was determined. Firstly, the local volumetric rate of photon absorption, W/m^3, at a specific depth is defined by Eq. (4):

$$LVRPA(z) = k_A \cdot C_{Fe} \cdot UV_o \cdot 10^{-k_A \cdot C_{Fe} \cdot (z/\cos\theta)} \quad (4)$$

By integrating over reactor depth, D, multiplying by the reactor surface (S_R) for incoming photons and dividing by the whole reactor volume (V_R), the VRPA per unit of volume was expressed in W/m^3 by:

$$VRPA = \frac{S_R}{V_R} \int_0^D k_A \cdot C_{Fe} \cdot UV_o \cdot 10^{-k_A \cdot C_{Fe} \cdot (z/\cos\theta)} dz \quad (5)$$

where averaged values of global UV irradiance, UV_o, and angle of incidence over the experimental time of each run were used for Eq. (5) computation.

2.4. Chemical analysis

The sample volume was 10 mL. All samples were immediately filtered (nylon filters from Millipore® with pores of 0.20 μm-diameter) and the filter was washed with acetonitrile in a

relationship acetonitrile: sample 1:10 and mixed with the filtered water sample. This is because acetonitrile acts as an HO• scavenger, stopping the reaction [31], and also sweeps out any trace of pollutant that may have been retained by the filter and avoid any possible adsorption.

Hydrogen peroxide was measured by a colorimetric method using ammonium metavanadate, measuring the absorbance at 450 nm [32]. The concentration of iron was determined according to the o-phenantroline standardised procedure (ISO 6332) and the red complex formed was determined spectrophotometrically at 510 nm. DOC determinations were carried out in a Shimadzu-V CPH TOC analyser. Anion concentrations were determined using ion chromatography (Metrohm 881 Compact IC pro). The eluent used was a solution of Na_2CO_3.

ACTM and TBZ concentrations were determined by means of liquid chromatography (UPLC Agilent 1200 Series equipped with a column oven, degasser, autosampler and diode array detector) with a reversed-phase column (Agilent XDB-C18). The mobile phase consisted of a gradient mixture of acetonitrile and 1% (v/v) formic acid in water. Retention times were 6.1 min for TBZ, 9.6 for ACTM. The detection wavelengths were 300 nm for TBZ and 248 nm for ACTM. The gradient used was initially set at 5% acetonitrile, progressively increasing the concentration to 100% in a 12-min method. The limit of detection (LOD) was 2 μg/L for ACTM and 1 μg/L for TBZ.

3. Results

A summary of the experimental conditions assayed is presented in Table 1, where iron concentration and liquid depth are operation variables and incident radiation, UV_o, is an environmental variable which depends on the day of the year and the time of day during experimentation. The volumetric rate of photon absorption was calculated by Eq. (5). Experimentation was carried out with the same initial concentration of hydrogen peroxide in all cases with excess at a low concentration (50 mg/L) so as not to limit the reaction rate and to avoid promoting inefficient reactions.

To illustrate the process performance, ACTM and TBZ at 100 μg/L each degradation profiles at an UV irradiance of 27 W/m^2 are shown in Fig. 4. In all the conditions tested, TBZ degradation rate was much faster than ACTM. Indeed, only with the lowest catalyst concentration (1 mg/L Fe) the reaction rate could be measured for both liquid depths. For 5.5 and 10 mg/L of Fe TBZ degradation was achieved in less than 2.5 min.

The explanation of the trend of the curves is based on the reported two-step kinetics for Fenton oxidation [33,34]. The

Table 1
Experimental conditions.

Fe (mg/L)	Depth (cm)	UV_o (W/m^2)	VRPA (W/m^3)
10.0	5	17	92
10.0	5	29	156
10.0	5	30	170
10.0	15	11	27
10.0	15	27	70
10.0	15	10	20
5.5	5	23	86
5.5	5	27	98
5.5	5	28	106
5.5	5	30	114
5.5	5	31	118
5.5	15	10	19
5.5	15	27	59
1.0	5	28	24
1.0	5	27	24
1.0	5	29	26
1.0	15	27	21
1.0	15	27	21

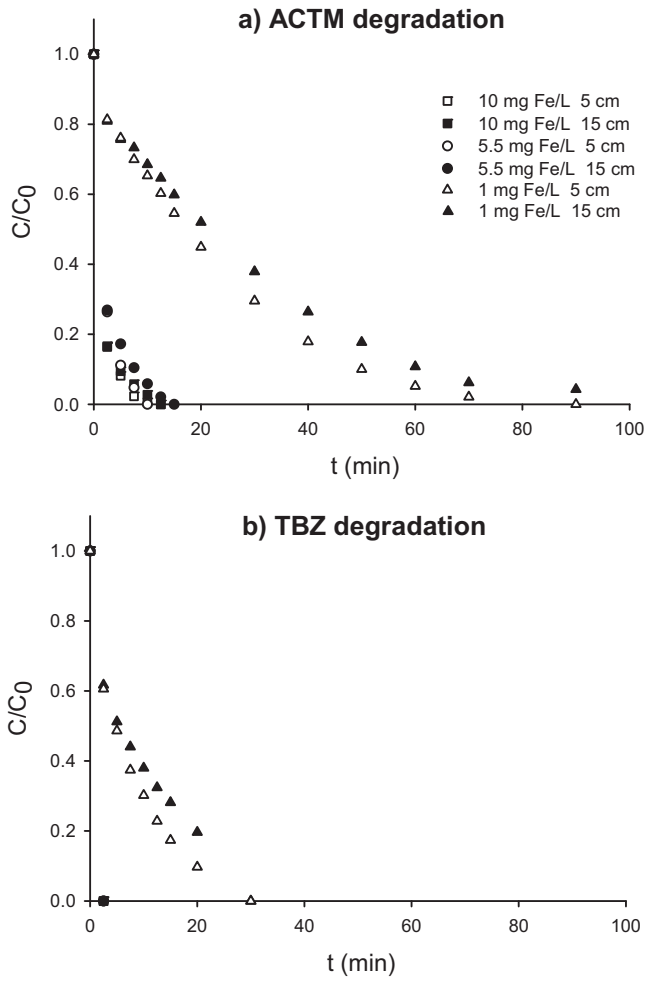

Fig. 4. ACTM (a) and TBZ (b) degradation profiles (100 μg/L each) with 1, 5.5 and 10 mg Fe/L in 5 and 15 cm liquid depth (27 W/m^2 UV irradiance).

experiments were started with the addition of hydrogen peroxide to the system, which already had the pesticide mixture and ferrous salt. The moment the oxidant was added, the Fenton reaction described in Eq. (6) took place. This reaction is very fast (76 M^{-1} s^{-1}) [35] and yields hydroxyl radicals, responsible for the initial ACTM and TBZ oxidation observed at the beginning of the experiments (Fig. 4). In the photo-Fenton process, ferric iron absorbs light, again yielding hydroxyl radicals and reducing ferric iron to ferrous iron (Eq. (7)). After that the redox cycle is established and since reaction represented in Eq. (7) is slower than in Eq. (6), the former is rate limiting [36].

$$Fe^{2+} + H_2O_2 \rightarrow Fe^{3+} + HO^- + HO^\bullet \quad (6)$$

$$Fe^{3+} + h\nu + H_2O \rightarrow Fe^{2+} + HO^\bullet + H^+ \quad (7)$$

The radicals react with the pesticides as follows (Eqs. (8) and (9)):

$$TBZ + HO^\bullet \rightarrow TP_{TBZ} \quad (8)$$

$$ACTM + HO^\bullet \rightarrow TP_{ACTM} \quad (9)$$

where TP_{TBZ} and TP_{ACTM} stand for transformation products from the parent molecules.

Increasing catalyst concentration always increased the reaction rate, regardless of the liquid depth. With 1 mg Fe/L, ACTM degradation was achieved in 90 min for both liquid depths; while TBZ was degraded in 30 min. With 5 cm and 5.5 and 10 mg/L Fe, ACTM was degraded in less than 15 min. With 15 cm liquid depth, degradation

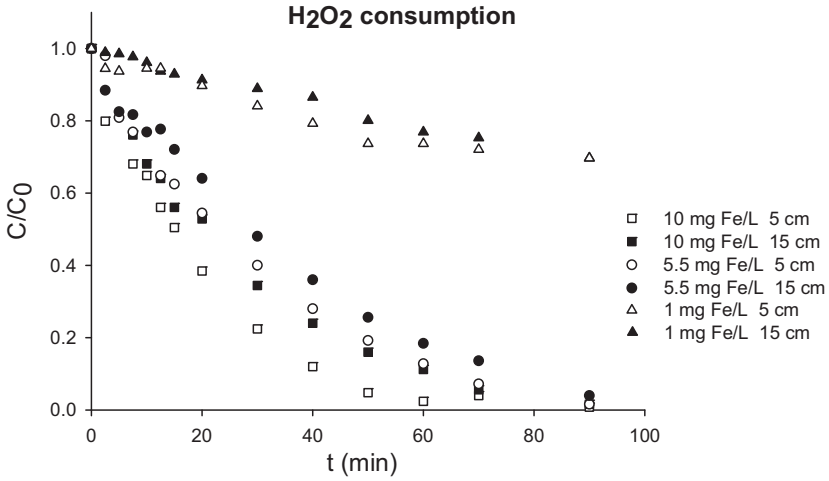

Fig. 5. Hydrogen peroxide consumption with 1, 5.5 and 10 mg Fe/L in 5 and 15 cm liquid depth (27 W/m^2 UV irradiance) when degrading ACTM and TBZ, 100 μg/L each.

rate was slightly higher with 10 mg/L Fe than with 5.5 mg/L Fe but not proportional to iron concentration.

Because TBZ was more reactive than ACTM and the latter displayed degradation curves in all the conditions assayed, ACTM was chosen as the target pollutant and the discussion below is focused on ACTM degradation, knowing that when ACTM was degraded, TBZ was also.

It is worth pointing out that pesticide degradation does not directly depend on irradiation but on the attack by HO• (Eqs. (8) and (9)). Therefore, there is an indirect dependence of pollutant removal on reactions represented in Eqs. (6) and (7). The variable that gives a better insight into the effect of photon absorption on pesticide removal is hydrogen peroxide consumption. It is directly dependent on photon-absorption through the iron redox cycle (Eqs. (6) and (7)). Therefore it is worth studying hydrogen peroxide consumption profiles, Fig. 5.

Hydrogen peroxide consumption increased with iron concentration. The effect of liquid depth was not significant for 1 mg/L Fe pointing out that there was enough photon availability to activate all the iron in solution. For 5.5 mg/L Fe and 10 mg/L Fe consumption rate was higher with 5 cm liquid depth than with 15 cm, thus the highest rate was obtained with 5 cm liquid depth and 10 mg/L Fe. In this case, photon availability limited the reaction rate because there was an excess of iron with respect to the photons entering the liquid. H_2O_2 was mostly consumed through reaction described in Eq. (6), which is cyclically dependent on reaction defined in Eq. (7) (ferric iron reduction by UV light). Therefore, the H_2O_2 reaction rate is irradiance and iron dependent.

4. Discussion

As described above, the consumption rate of H_2O_2 was considered dependent on Fe concentration and light availability, which is related to irradiance on the reactor surface and liquid depth. To study the effect of irradiance on process kinetics, the concept of VRPA described in Section 2.3 was used.

The rearrangement of reactions represented in Eqs. (6) and (7) gives rise to Eq. (10), where the direct relationship between hydrogen peroxide consumption and the VRPA can be seen.

$$H_2O_2 + H_2O + \text{VRPA} \xrightarrow{\text{Fe}} 2HO^{\bullet} + HO^- + H^+ \quad (10)$$

Consequently, the following apparent first order rate law was applied:

$$-\frac{d[H_2O_2]}{dt} = k_{H_2O_2} \cdot [H_2O_2] \quad (11)$$

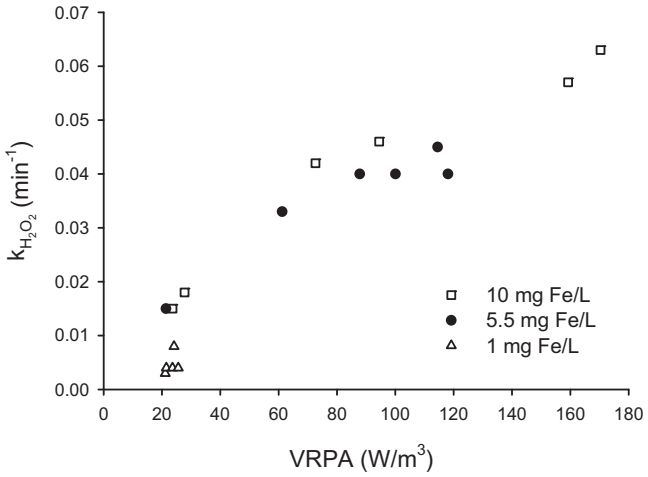

Fig. 6. Effect of the VRPA on hydrogen peroxide pseudo-first order kinetic constant for each iron concentration.

where

$$k_{H_2O_2} = f(\text{Fe}, \text{VRPA})$$

Fig. 6 illustrates the change in $k_{H_2O_2}$ with photon absorption with iron concentration as the parameter. For 1 mg/L Fe, little variation was observed due to the narrow range in VRPA's values. This is due to the dependence of VRPA on iron concentration. For 5.5 mg/L Fe, the apparent kinetic constant reached a stable value of around 0.042 min^{-1} for VRPA ~90–120 W/m^3, pointing out an irradiance saturation effect. This meant that the hydrogen peroxide consumption rate would not increase despite increasing the VRPA above 90 W/m^3 because there were enough photons to photoactivate all the iron in solution. For the highest iron concentration assayed, 10 mg Fe/L, the kinetic constant variation with VRPA matched that obtained for 5.5 mg/L up to ~90 W/m^3 but the values still increased for photon absorption rates higher than 150 W/m^3. In this case, irradiance saturation took place at a higher VRPA level since there were more iron ions in solution.

As a result, $k_{H_2O_2}$ was not a linear function of VRPA. As far as the authors know, the observed phenomenon has not been previously reported and more research on reaction mechanism is necessary. Therefore, a mathematical hyperbolic relationship has been proposed to take into account the observed kinetic saturation effect, Eq. (12). Very often used in photocatalysis when interpreting

Table 2
Kinetic parameters for the saturation model.

Fe (mg/L)	k_m (min^{-1})	k_s (W/m^3)
10.0	0.136	186
5.5	0.077	87
1.0	0.014	18

saturation effects (adaptations of Langmuir–Hinshelwood kinetics), but very often also far from interpretation of mechanisms. Useful design equations may be obtained by the application of a Langmuir–Hinshelwood type model, even if in spite of it not fitting with the photo-Fenton reaction mechanism. By now, these equations must be obtained at pilot plant size, however, they will be useful for larger plants if the same type of collector is use [37].

$$k_{H_2O_2} = \frac{k_m \cdot \mathrm{VRPA}}{k_s + \mathrm{VRPA}} \quad (12)$$

where k_m (min^{-1}) stands for the maximum apparent kinetic constant and k_s (W/m^3) stands for the saturation constant. This means that the higher k_m, the higher photon absorption rate to activate all the iron in solution.

Therefore, since the radiant power absorbed in the raceway per volume unit depends on the amount of iron in solution, the hyperbolic model was applied for each iron concentration. Table 2 shows the kinetic parameters k_m and k_s calculated from the linearisation of Eq. (12) for 5.5 and 10 mg Fe/L, Eqs. (13)–(15):

$$\frac{1}{k_{H_2O_2}} = \frac{1}{k_m} + \frac{k_s}{k_m}\frac{1}{\mathrm{VRPA}} \quad (13)$$

$$\frac{1}{k_{H_2O_2}} = 13.05 + 1140\frac{1}{\mathrm{VRPA}} \quad r^2 = 0.994 \quad \text{for 5.5 mg Fe/L} \quad (14)$$

being 0.99 and 45.74 the standard errors at 95% confidence level for the intercept and the slope, respectively.

$$\frac{1}{k_{H_2O_2}} = 7.34 + 1367\frac{1}{\mathrm{VRPA}} \quad r^2 = 0.995 \quad \text{for 10 mg Fe/L} \quad (15)$$

being 1.15 and 47.66 the standard errors at 95% confidence level for the intercept and the slope, respectively.

As such, the mathematical model was consistent with the experimental observations. The low variation found in $k_{H_2O_2}$ and VRPA with 1 mg/L Fe prevented the direct application of the linear fit to experimental results. Nonetheless, based on the linear correlation between k_m and k_s with Fe concentration from zero to ten mg/L, the values shown in Table 2 for 1 mg/L Fe were calculated by linear interpolation.

Regarding ACTM degradation, the profiles in Fig. 4a show that the oxidation of ACTM occurs in a two-step reaction: ACTM is degraded very quickly in the first 2 min; then proceeds at a slower reaction rate. Due to the high concentration of hydroxyl radical generated during the first few minutes by the reaction described in Eq. (6), ACTM degradation rate during this first step followed a pseudo first order reaction, where the apparent kinetic constant, k_{1ACTM}, depended on the iron concentration. Consequently, the relationship between k_{1ACTM} and iron concentration was determined by means of a set of 2-min assays. In these assays, initial ACTM degradation rate was measured with iron concentrations of 2, 4, 6, 8 and 10 mg/L and 50 mg/L H_2O_2. According to these results, the apparent first order kinetic constant in step 1 was:

$$k_{1ACTM} = 6.1C_{Fe} \quad r^2 = 0.995 \quad (16)$$

where k_{1ACTM} is expressed in min^{-1} and C_{Fe} in mM. The standard error at 95% confidence level for the slope was 0.09.

The second reaction step was irradiance dependent (Eq. (7)) and due to the very low concentration of ACTM compared with iron and hydrogen peroxide dosage, an apparent first order rate law

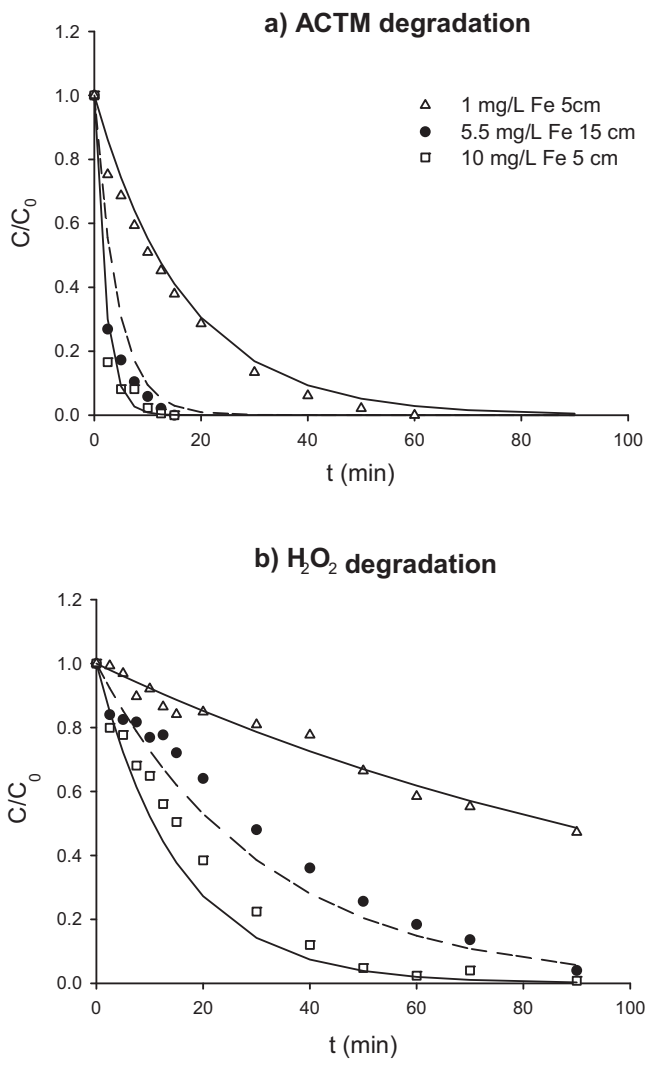

Fig. 7. Model validation for ACTM and hydrogen peroxide profiles with 1, 5.5 and 10 mg Fe/L in 5 cm and 15 cm.

for ACTM degradation was also applied with the kinetic constant k_{2ACTM}. In this case, the progressive generation of hydroxyl radicals depended directly on the hydrogen peroxide reaction rate. Consequently, a linear relationship was observed between k_{2ACTM} and $k_{H_2O_2}$, Eq. (17):

$$k_{2ACTM} = 7.4k_{H_2O_2} \quad r^2 = 0.951 \quad (17)$$

where both kinetic constants are expressed in min^{-1}. The standard error at 95% confidence level for the slope was 0.25.

For the purpose of modelling pesticide degradation and hydrogen peroxide consumption, $k_{H_2O_2}$ was estimated with Eq. (12) for each iron concentration, irradiance and liquid depth. As for ACTM, k_{1ACTM} was estimated with Eq. (16) and applied for the two first minutes of reaction; k_{2ACTM} was estimated with Eq. (17) and applied from minute 2 until the end of the run. The results of the model are shown in Fig. 7. The model provides an acceptable fit for both variables, and behaviour compatible with the assumption of a photon absorption saturation effect.

Additionally, the model for ACTM degradation was used to estimate the treatment capacity (TC) of the RPR, expressed as the mass of ACTM removed per unit of time and surface of reactor exposed to radiation, mg/h m^2. This is a degradation rate taking into account photoreactor exposure to sunlight which takes into account that the treated volume changes with depth. The treatment capacity

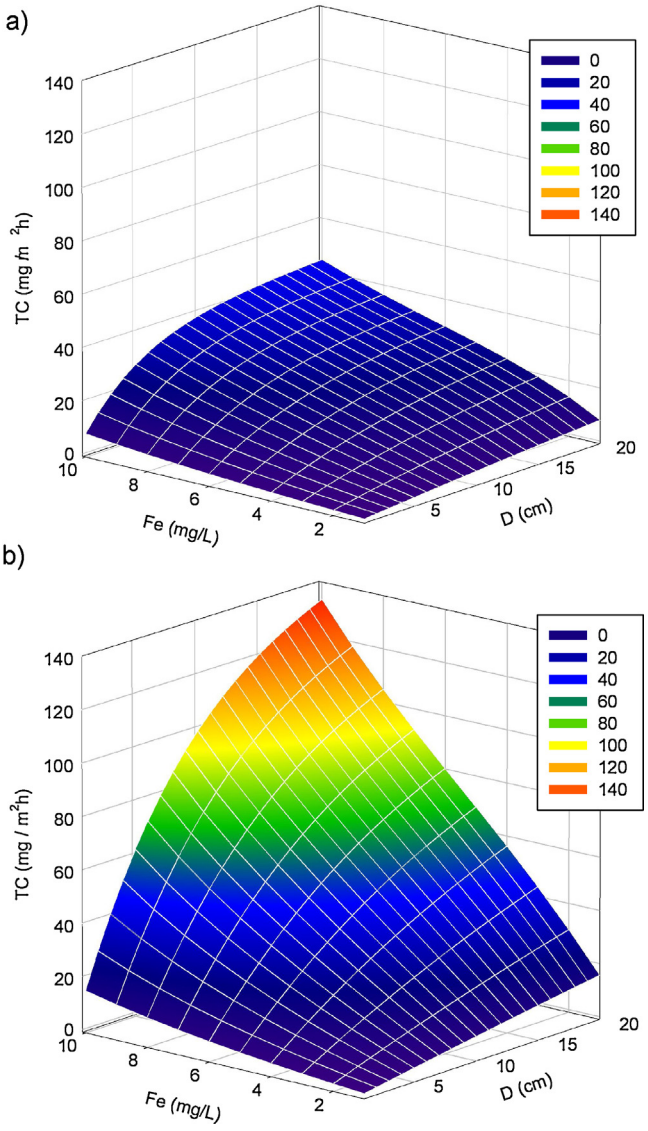

Fig. 8. Treatment capacity as a function of iron concentration and liquid depth for two representative days at noon. (a) $UV_o = 10\,W/m^2$, $\theta = 0.902$ rad, Julian Day 38; (b) $UV_o = 30\,W/m^2$, $\theta = 0.284$ rad, Julian Day 142.

was estimated with the model up to 20 cm liquid depth. The optical thickness, τ, was calculated as follows:

$$\tau = k_A \cdot C_{Fe} \cdot D \tag{18}$$

For $D = 20$ cm and 10 mg/L iron concentration optical thickness was 1.82. It has been reported that for photocatalytical reactors the optimal value of τ is between 1.8 and 3.4 [38]. An optical thickness of 1.82 ensures the system was illuminated at the bottom of the reactor with 20 cm liquid depth.

Treatment capacity was estimated by:

$$TC = \frac{0.99 ACTM_0 V_R}{S_R t} \tag{19}$$

where t is the calculated reaction time to reach 99% ACTM removal.

In Fig. 8, the variation in TC as a function of iron concentration and liquid depth is shown for two irradiances. In both cases, TC increases with catalyst concentration and depth; but although TC is higher for the higher irradiance, the variation pattern significantly varies with irradiance level. For $10\,W/m^2$, representative of a run carried out in February, liquid depth does not have a strong effect on TC when iron concentration is low. Only for high iron concentration, does TC initially increase with depth and then stabilise at around a value of 40 mg/h m^2 for 10 cm liquid depth or deeper with 10 mg/L Fe. This TC plateau is related to the Fenton effect due to the first oxidation of the dosed ferrous iron (Reaction described in Eq. (6)) which causes a drop in ACTM concentration, independent of light availability. This means that at low irradiances it is not worth using large water volumes as it increases mixing costs. On the other hand, for $30\,W/m^2$ the dependence of TC on depth at high iron concentrations is remarkable. At low depth, for instance 5 cm, TC is 62 mg/h m^2 and increases up to 120 mg/h m^2 for 15 cm reaching 133 mg/h m^2 for 20 cm liquid depth. These results highlight the importance of setting the liquid depth for irradiance on reactor surface to improve RPR performance. Under low irradiances, mild operating conditions (5 mg/L Fe are commonly reported for micropollutant removal) could be used with a low volume of water per surface unit, of around $100\,L/m^2$. However, under high irradiances the RPR would be operated with greater depths and higher iron concentrations to make the most of photons entering the reactor, increasing the volume of water per surface unit up to $200\,L/m^2$.

5. Conclusions

RPRs have proved to be a feasible technology for micropollutant removal. They allow high treatment capacity (40–133 mg/h m^2), dependent on the yearly season and irradiance variation. A mathematical model could be adjusted to predict micropollutant degradation, taking into account photon absorption and irradiance saturation effects. The model allows predicting the operating conditions (iron concentration and liquid depth) as a function of irradiance. The simulation indicated that the photoreactor could be operated up to 20 cm liquid depth ($200\,L/m^2$).

Acknowledgements

This research was supported by the Junta de Andalucía (Andalusian Regional Government) P10-RNM-05951, the Ministerio de Economía y Competitividad (Spanish Government) CTQ2013-46398-R; and the European Regional Development Fund (ERDF). Gracia Rivas Ibáñez would like to acknowledge the Junta de Andalucía for her FPI scholarship. Irene Carra would like to acknowledge the Ministerio de Educación, Cultura y Deporte for her FPU scholarship (AP2010-3218).

References

[1] K.J. Bisceglia, J.T. Yu, M. Coelhan, E.J. Bouwer, A.L. Roberts, J. Chromatogr. A 1217 (2010) 558–564.
[2] M.L. Ballesteros, K.S.B. Miglioranza, M. Gonzalez, G. Fillmann, D.A. Wunderlin, M.A. Bistoni, Sci. Total Environ. 490 (2014) 73–80.
[3] A. Azzouz, B. Souhail, E. Ballesteros, J. Chromatogr. A 1217 (2010) 2956–2963.
[4] J. Robles-Molina, F.J. Lara-Ortega, B. Gilbert-López, J.F. García-Reyes, A. Molina-Díaz, J. Chromatogr. A 1350 (2014) 30–43.
[5] M. Köck-Schulmeyer, M. Villagrasa, M. López de Alda, R. Céspedes-Sánchez, F. Ventura, D. Barceló, Sci. Total Environ. 458–460 (2013) 466–476.
[6] Y. Luo, W. Guo, H.H. Ngo, L.D. Nghiem, F.I. Hai, J. Zhang, S. Liang, X.C. Wang, Sci. Total Environ. 473–474 (2014) 619–641.
[7] M. Kuster, M.J. López de Alda, M.D. Hernando, M. Petrovic, J. Martín-Alonso, D. Barceló, J. Hydrol. 358 (2008) 112–123.
[8] R. Moreno-González, S. Rodríguez-Mozaz, M. Gros, E. Pérez-Cánovas, D. Barceló, V.M. León, Sci. Total Environ. 490 (2014) 59–72.
[9] S. Koenig, D. Huertas, P. Fernández, Sci. Total Environ. 443 (2013) 358–366.
[10] R. Van Aerle, M. Nolan, S. Jobling, L.B. Christiansen, J.P. Sumpter, C.R. Tyler, Environ. Toxicol. Chem. 20 (2001) 2841–2847.
[11] A. Bernabeu, R.F. Vercher, L. Santos-Juanes, P.J. Simón, C. Lardín, M.A. Martínez, J.A. Vicente, R. González, C. Llosá, A. Arques, A.M. Amat, Catal. Today 161 (2011) 235–240.
[12] N. Klamerth, S. Malato, A. Agüera, A. Fernández-Alba, Water Res. 47 (2013) 833–840.
[13] H. Kusic, N. Koprivanac, S. Horvat, S. Bakija, A.L. Bozic, Chem. Eng. J. 155 (2009) 144–154.

[14] S.M. Rodríguez, J.B. Gálvez, M.I.M. Rubio, P.F. Ibáñez, D.A. Padilla, M.C. Pereira, J.F. Mendes, J.C. De Oliveira, Solar Energy 77 (2004) 513–524.
[15] G.H. Rossetti, E.D. Albizzati, O.M. Alfano, Solar Energy 77 (2004) 461–470.
[16] J. Colina-Márquez, F. MacHuca-Martínez, G.L. Puma, Environ. Sci. Technol. 44 (2010) 5112–5120.
[17] S. Malato, P. Fernández-Ibáñez, M.I. Maldonado, J. Blanco, W. Gernjak, Catal. Today 147 (2009) 1–59.
[18] I. Carra, J.L. García Sánchez, J.L. Casas López, S. Malato, J.A. Sánchez Pérez, Sci. Total Environ. 478 (2014) 123–132.
[19] F.G. Acién Fernández, J.M. Fernández Sevilla, E. Molina Grima, Rev. Environ. Sci. Biotechnol. 12 (2013) 131–151.
[20] Y. Chisti, Biotechnol. Adv. 25 (2007) 294–306.
[21] E. Neyens, J. Baeyens, J. Hazard. Mater. 98 (2003) 33–50.
[22] A. Bernabeu, S. Palacios, R. Vicente, R.F. Vercher, S. Malato, A. Arques, A.M. Amat, Chem. Eng. J. 198–199 (2012) 65–72.
[23] N. De la Cruz, J. Giménez, S. Esplugas, D. Grandjean, L.F. De Alencastro, C. Pulgarín, Water Res. 46 (2012) 1947–1957.
[24] J. Fitzgerald, C. Jay, Crop Prot. 30 (2011) 1178–1183.
[25] J.F. García-Reyes, B. Gilbert-López, A. Molina-Díaz, A.R. Fernández-Alba, Anal. Chem. 80 (2008) 8966–8974.
[26] J. Gomis, A. Bianco Prevot, E. Montoneri, M.C. González, A.M. Amat, D.O. Mártire, A. Arques, L. Carlos, Chem. Eng. J. 235 (2014) 236–243.
[27] R. Zhang, S. Vigneswaran, H. Ngo, H. Nguyen, Desalination 216 (2007) 325–333.
[28] J.A. Duffie, W.A. Beckman, Solar Engineering of Thermal Processes, 4th ed., 2013.
[29] O.M. Alfano, H.A. Irazoqui, A.E. Cassano, Photochem. Photobiol. Sci. 8 (2009) 1047–1058.
[30] J. Farias, E.D. Albizzati, O.M. Alfano, Catal. Today 144 (2009) 117–123.
[31] S. Mitroka, S. Zimmeck, D. Troya, J.M. Tanko, J. Am. Chem. Soc. 132 (2010) 2907–2913.
[32] R.F.P. Nogueira, M.C. Oliveira, W.C. Paterlini, Talanta 66 (2005) 86–91.
[33] L.I. Doumic, P.M. Haure, M.C. Cassanello, M.A. Ayude, Appl. Catal. B: Environ. 142–143 (2013) 214–221.
[34] J.H. Ramirez, F.M. Duarte, F.G. Martins, C.A. Costa, L.M. Madeira, Chem. Eng. J. 148 (2009) 394–404.
[35] R. Chen, J.J. Pignatello, Environ. Sci. Technol. 31 (1997) 2399–2406.
[36] J.J. Pignatello, E. Oliveros, A. MacKay, Crit. Rev. Environ. Sci. Technol. 36 (2006) 1–84.
[37] S. Malato, J. Blanco, C. Richter, M.I. Maldonado, Appl. Catal. B: Environ. 25 (2000) 31–38.
[38] G. Li Puma, Environ. Sci. Technol. 37 (2003) 5783–5791.